







## Hydrothermal ferromanganese oxides around a petit-spot volcano on old and cold oceanic crust

Keishiro Azami <sup>1,7,8✉</sup>, Shiki Machida <sup>2</sup>, Naoto Hirano <sup>3✉</sup>, Kentaro Nakamura<sup>1,2,4</sup>, Kazutaka Yasukawa <sup>1,4</sup>, Tetsu Kogiso <sup>5</sup>, Masao Nakanishi <sup>6</sup> & Yasuhiro Kato <sup>1,2</sup>

Areas of old and cold oceanic plate lack conventional volcanism and have been assumed to be devoid of submarine hydrothermal activity. However, petit-spot volcanoes are common in areas of flexure of such oceanic plates. Here, we report hydrothermal ferromanganese oxides dredged from the vicinity of a petit-spot volcano at 5.7 km water depth in an area of oceanic plate flexure east of the Japan Trench. The bulk chemical, lead isotopic and mineralogical compositions of the samples indicate their formation by low-temperature hydrothermal activity, which can be interpreted as being caused by fluid–rock interactions at <200 °C. We propose that interaction of local marine sediments with volatile-rich petit-spot magmas may produce hydrothermal fluids containing not only iron and manganese but also enough amounts of carbon dioxide and methane to have implications for the global carbon cycle. However, contemporary hydrothermal activities at petit-spot volcanoes have not been confirmed yet.

<sup>1</sup>Department of Systems Innovation, School of Engineering, The University of Tokyo, 7-3-1 Hongo, Bunkyo-ku, Tokyo 113-8656, Japan. <sup>2</sup>Ocean Resources Research Center for Next Generation, Chiba Institution of Technology, 2-17-1 Tsudanuma, Narashino, Chiba 275-0016, Japan. <sup>3</sup>Center for Northeast Asian Studies, Tohoku University, 41 Kawauchi, Aoba-ku, Sendai 980-8576, Japan. <sup>4</sup>Frontier Research Center for Energy and Resources, School of Engineering, The University of Tokyo, 7-3-1 Hongo, Bunkyo-ku, Tokyo 113-8656, Japan. <sup>5</sup>Graduate School of Human and Environmental Studies, Kyoto University, Yoshida-nihonmatsu, Sakyo, Kyoto 606-8501, Japan. <sup>6</sup>Graduate School of Science, Chiba University, 1-33 Yayoi-cho, Inage-ku, Chiba 263-8522, Japan. <sup>7</sup>Present address: School of Creative Science and Engineering, Waseda University, 3-4-1 Okubo, Shinjuku-ku, Tokyo 169-8555, Japan. <sup>8</sup>Present address: Ocean Resources Research Center for Next Generation, Chiba Institution of Technology, 2-17-1 Tsudanuma, Narashino, Chiba 275-0016, Japan. ✉email: [k.azami@aoni.waseda.jp](mailto:k.azami@aoni.waseda.jp); [nhirano@tohoku.ac.jp](mailto:nhirano@tohoku.ac.jp)

Submarine volcanism supplies multiple elements to the oceanic environment. Submarine hydrothermal systems, which have been documented at depths of up to 4960 m<sup>1</sup>, produce hydrothermal deposits and hydrothermally alter the oceanic crust<sup>2–4</sup>. They play an important role in the geochemical budget of the ocean. Elemental fluxes from hydrothermal systems, estimated from the water volume flux and hydrothermal fluid chemistry, are considered important parameters for modeling biogeochemical cycles and chemosynthetic ecosystems<sup>3,5–7</sup>. Although elemental fluxes from hydrothermal systems in mid-ocean ridge (MOR) settings have been extensively studied<sup>3,4</sup>, the reliable estimations of global elemental fluxes from hydrothermal vents, including those in low-temperature systems (<150 °C), remains difficult because of uncertainties in water volume flux and hydrothermal fluid chemistry<sup>3,6,8</sup>. Water volume fluxes from low-temperature hydrothermal systems are particularly uncertain because these systems are difficult to detect using conventional physicochemical sensors<sup>8</sup>. Although previous researchers have implied that such fluxes might influence estimations of elemental fluxes in the ocean<sup>8</sup>, accurate estimates are hindered by large variations in the chemistry of low-temperature hydrothermal fluids, particularly in tectonic settings such as back-arc systems<sup>5</sup>. Therefore, to accurately understand the role of submarine hydrothermal systems in biogeochemical cycles and chemosynthetic ecosystems, it is important to identify hydrothermal systems that affect elemental fluxes in the ocean under such specific tectonic settings.

Here, we suggest that areas of petit-spot volcanoes are a specific tectonic setting that can affect elemental fluxes in the ocean. Petit-spot volcanoes are small monogenetic edifices reported in intra-plate settings that are subjected to plate flexure<sup>9,10</sup>. They have been documented in multiple parts of oceans worldwide<sup>10</sup> and are expected to exhibit hydrothermal activity. Interestingly, petit-spot volcanoes erupt magmas of asthenospheric origin<sup>9,11</sup> that are highly enriched in volatiles (especially CO<sub>2</sub>)<sup>12</sup>. The estimated CO<sub>2</sub> flux from petit-spot volcanic edifices is 0.1–1.2% comparing to that from Earth's entire MOR system<sup>12</sup>. However, numerous intrusions of petit-spot magma into sedimentary layers that have been recognized in recently acquired seismic survey data<sup>13</sup> suggest that the flux estimated above is a lower limit. Despite its small volume<sup>14</sup>, therefore, petit-spot volcanism could have a measurable effect on the global carbon cycle. CO<sub>2</sub> derived from magmatic fluids has been shown to reduce the pH and increase the alkalinity of hydrothermal fluids<sup>15</sup>, thus promoting the leaching of lava, even at low temperatures. Petit-spot volcanoes produce peperite<sup>16</sup>, a conglomerate of lava fragments and baked mud formed during water-rich sediment–magma interactions. Because the peperite formation can involve methanogenesis in sediments by thermal decomposition of organic matter and/or microbial activity in response to variable temperature<sup>5</sup>, the petit-spot hydrothermal fluids possibly contain CH<sub>4</sub>. Thus, although petit-spot volcanoes have not been recognized as hydrothermally active sites, we propose that their hydrothermal outflow not only contributes elemental fluxes to the ocean but may provide habitable settings for chemosynthetic communities.

During cruise KS-18-9 of R/V *Shinsei-maru* in 2018, we recovered samples of ferromanganese (Fe–Mn) oxides of ~3.5 cm thickness and petit-spot lavas by dredge on a petit-spot volcano on the outer rise of the Japan Trench in the northwestern (NW) Pacific Ocean at water depths of 5719–5707 m (Fig. 1). These Fe–Mn oxide samples have a dull metallic luster and are not accompanied by substrate rocks or cores (Fig. 2). These features clearly distinguish them from the Fe–Mn oxides of hydrogenetic origin previously reported from petit-spot volcanoes<sup>17</sup>. Although the basaltic crust of the study area is extremely old (~131 Ma)<sup>18</sup>, the alteration rind (palagonite) of glassy petit-spot lava samples is

<1 mm thick. Assuming a palagonitization rate of 3–20 μm/kyr for basaltic glass in seawater<sup>19</sup>, the eruption of this petit-spot volcano was younger than 0.33 Ma, thus representing one of the youngest known petit-spot volcanoes on the NW Pacific plate<sup>9,14</sup>.

To identify the origins of the Fe–Mn oxides, we analyzed the mineral, chemical, and Pb isotopic compositions of eight Fe–Mn oxide samples obtained during the cruise KS-18-9. Two samples were analyzed for their elemental distributions by using micro-X-ray fluorescence (micro-XRF), and independent component analysis (ICA) of micro-XRF mapping data was conducted to examine the formation process.

## Results

Eight Fe–Mn oxide samples were powdered for bulk chemical and mineralogical analyses. Out of these samples, three samples presenting a thin rim (<2 mm) of overgrown Fe–Mn oxides to the naked eye were cut into two subsamples with and without the rim material and then powdered. Elemental maps of split and polished samples demonstrate anticorrelated Mn and Fe and demonstrate that silicate debris (as reported in images of Si) is cemented by Fe–Mn oxides (Fig. 2)<sup>20</sup>. The rim material exhibits a columnar structure that is typical of hydrogenetic Fe–Mn crusts.

The bulk chemical compositions of these samples without overgrown rims are characterized by high concentrations of Fe and Mn (Mn/Fe = 1.1–3.5) and low concentrations of Co, Ni, and Cu; high field strength elements; and rare-earth elements plus Y (REY) (Supplementary Table 1)<sup>21</sup>. Chondrite-normalized<sup>22</sup> REY patterns show negative Eu anomalies (Fig. 3). The samples, including those with portions of the rim, have higher trace element contents than their counterparts without the rim, and they exhibit negative Y/Ho anomalies.

X-ray diffraction (XRD) patterns of powdered samples (Supplementary Fig. 1)<sup>23</sup> show peaks corresponding to birnessite (7-Å manganate), smectite, quartz, and plagioclase. Vernadite (δ-MnO<sub>2</sub>) was reported only in samples that include rim material (Supplementary Table 1)<sup>21</sup>.

We obtained Pb isotopic compositions in the Fe–Mn oxide samples, petit-spot lava samples from the study area, and presently forming hydrogenetic Fe–Mn crusts (surface layers of <5 mm thick) from the Joban Seamounts of offshore northeastern (NE) Japan and Ojin Rise Seamounts east of Shatsky Rise in NW Pacific Ocean. The Fe–Mn samples were leached with HCl to determine the Pb isotopic compositions of ambient seawater at the time of formation. Pb isotopic compositions of our Fe–Mn oxide samples differ from those of petit-spot lavas, but they resemble those of presently forming hydrogenetic Fe–Mn crusts (Fig. 4 and Supplementary Table 2)<sup>21</sup>.

## Discussion

**Geochemical evidence of petit-spot hydrothermal activity.** The characteristics of submarine Fe–Mn oxide are depicted here in a geochemical ternary diagram<sup>24</sup>. Most samples plot within the hydrothermal origin field; however, the rimmed samples lie between the hydrothermal and intermediate hydrogenetic and diagenetic fields (Fig. 5). Because Fe–Mn crusts grow only on hard rocks, they are considered to be formed hydrogenetically, rather than by early diagenesis of soft sediments (diagenetic origin). However, in oceans where there is abundant supply of terrigenous detritus, the chemical composition of Fe–Mn crusts can show minorly diagenetic features, making them richer in Ni and Cu than typical hydrogenetic Fe–Mn crusts (possibly associated with bioproductivity near the ocean surface)<sup>17,25–27</sup> (Fig. 5). Thus, the rim material we studied is considered to reflect the characteristics of hydrogenetic Fe–Mn oxides formed in an ocean with a high terrigenous detrital supply. Birnessite and

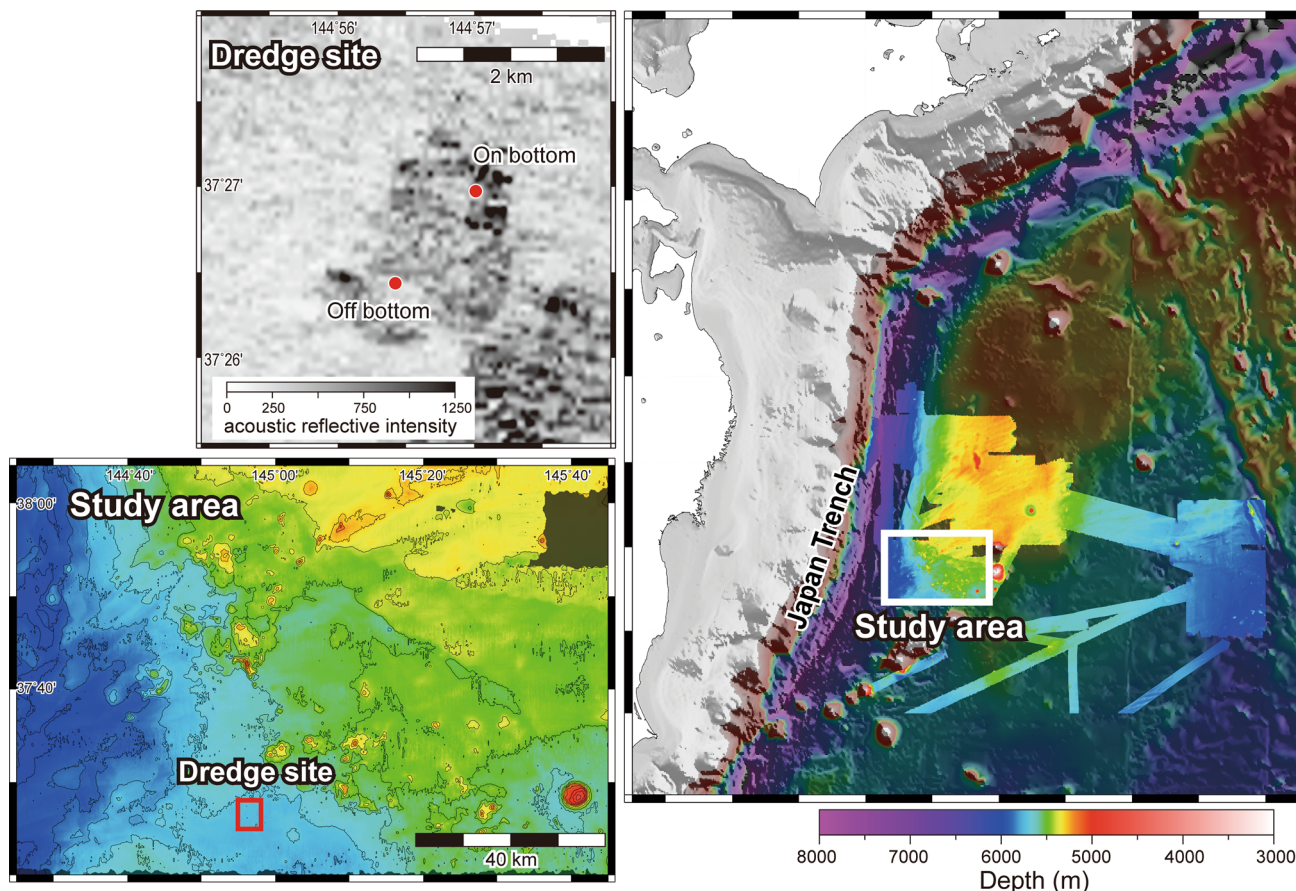


**Fig. 1** Maps of the study area. The study area is at the outer rise of the Japan Trench (white box in the right map). The red box in the lower-left map delineates the dredge site (D05 dredge of the cruise KS-18-9); contour interval = 100 m. In the topographic maps, brighter colors delineate areas surveyed by research cruises KR03-07, KR04-08, YK05-06, KR07-06, and KR07-07. Topographic data for other areas are from ETOPO1<sup>67</sup>. Because petit-spot volcanoes are difficult to recognize from bathymetric data, the petit-spot volcano in this study was recognized on a gray-scale map of acoustic reflective intensities measured during the YK11-E05 cruise (the upper-left map). The on-bottom and off-bottom points of the dredge are located in the area of high acoustic reflective intensity, indicating a petit-spot volcano. All maps were prepared using GMT software<sup>68</sup>.

vernadite detected in the samples are consistent with the geochemical discrimination. Unstable todorokite (10 Å manganate), which is precipitated from low-temperature hydrothermal fluids, is detected as birnessite in dried samples<sup>28</sup>. The rim samples contain vernadite, which is of hydrogenetic origin. These results show that the samples precipitated from low-temperature hydrothermal fluids and demonstrate a hydrogenetic rim after the cessation of hydrothermal activity.

Petit-spot volcanoes are the potential heat source for such hydrothermal activity in our study area, where any volcanisms, except for recent petit-spot volcanoes<sup>9,10</sup>, have not recognized since the formation of the oceanic plate in MOR at ~131 Ma<sup>18</sup>. The hydrogenetic rims (<2 mm) we observed on the samples are not inconsistent with a hydrothermal origin associated with a petit-spot volcano (<0.33 Ma) because the high growth rates (>20 mm/Myr) of hydrogenetic Fe–Mn oxides reported from the study area<sup>29</sup> with high supply of terrigenous detritus indicate the young age (<0.1 Ma) of the hydrogenetic rims. Therefore, we consider that hydrothermal activity associated with the petit-spot volcano is the most plausible phenomenon having formed the samples.

As the hydrogenetic rim of the samples indicates the cessation of hydrothermal activity, water depth of the dredge site (5707–5719 m) is different from water depth when hydrothermal activity occurred. However, even assuming plate motion after the formation of a petit-spot volcano (<0.33 Ma), a petit-spot volcano

had erupted at deeper than any other reported hydrothermal site (<4960 m)<sup>1</sup>. Because petit-spot volcanism occurs on old oceanic crust prior to subduction, it occurs at greater water depths than any other volcanic zone. Therefore, the deepest hydrothermal fields on Earth should occur in such a tectonic setting.

The chemical compositions of these samples also show low-temperature hydrothermal activity. Note that Mo shows high concentrations only in hydrothermal fluid-leached rocks at high temperatures (>310 °C)<sup>30</sup>. In hydrothermal systems, Mo is taken into either sulfide or Mn oxide. Consequently, high Mo contents in hydrothermal Fe–Mn oxides indicate high-temperature fluid–rock interactions, with the exception of contexts in which such reactions are accompanied by large-scale precipitation of sulfide before Mn oxide precipitation, such as at MORs. The lower Mo/Mn ratios of the samples without rim material ( $0.53 \times 10^{-3}$ – $1.34 \times 10^{-3}$ ) relative to volcanic arc<sup>31</sup>, back arc<sup>32</sup>, and hot spot<sup>33</sup> samples ( $0.27$ – $5.42 \times 10^{-3}$ ,  $0.93$ – $5.00 \times 10^{-3}$ , and  $0.22$ – $2.51 \times 10^{-3}$ , respectively) indicate that fluid–rock interactions occurred at lower temperatures (box plot in Supplementary Fig. 2). REY patterns can indicate fluid–rock interactions. Hydrothermal fluids interacting with rocks at temperatures of >200 °C result in the development of a positive Eu anomaly because  $\text{Eu}^{3+}$  in rocks is easily reduced to  $\text{Eu}^{2+}$ , which is readily dissolved<sup>34</sup>. Because the REY pattern of hydrothermal Fe–Mn oxides generally shows the composition of ambient water (mixture of seawater and hydrothermal fluid) during precipitation, positive Eu anomalies indicate high-

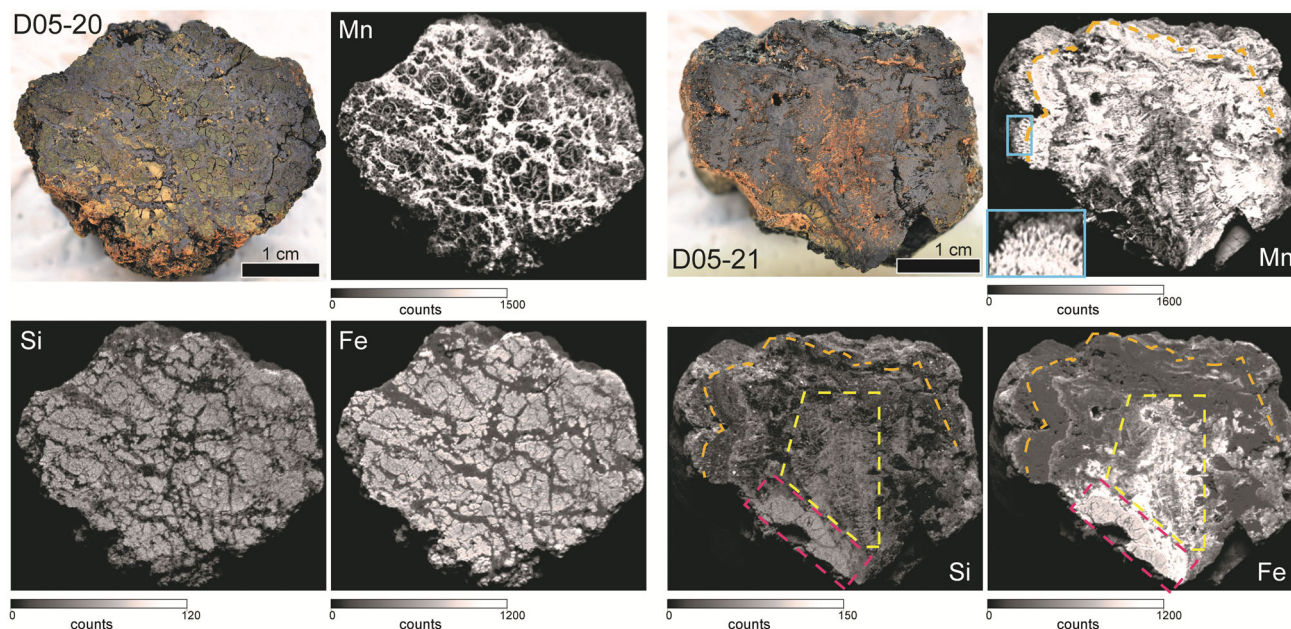


**Fig. 2 Sample images and micro-X-ray elemental mapping images.** The orange-dashed line on sample D05-21 shows the contact between the rim of overgrown Fe–Mn oxides and hydrothermal Fe–Mn oxides. The rim shows a columnar microstructure in the Mn map (inset). The samples show Mn and Fe decoupling with silicate debris (Si) cemented by Fe–Mn oxides, typifying hydrothermal Fe–Mn oxides on sediment-covered seafloors<sup>31</sup>. In D05-21, Fe and Si show different spatial distributions (lower Si intensity in the yellow-dashed area than in the red-dashed area regardless of the high intensity of Fe in both areas).

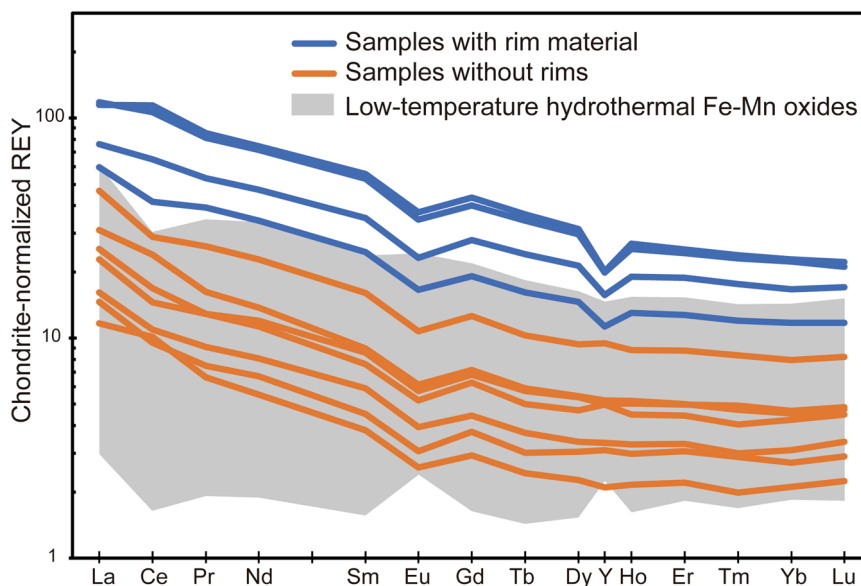


**Fig. 3 Chondrite-normalized REY compositions.** Blue lines show samples featuring overgrown rims; orange lines show the same samples with the rims excluded plus the remaining samples that had no rims. The gray field shows the compositional range of low-temperature hydrothermal Fe–Mn oxides from the Izu-Ogasawara arc<sup>36</sup> (mean  $\pm 1\sigma$ ). The absence of positive Eu anomalies indicates that fluid–rock interactions occurred at temperatures of  $<200$  °C. The C1-chondrite composition is from Anders and Grevesse<sup>69</sup>.

temperature fluid–rock interactions<sup>35,36</sup>. Indeed, positive Eu anomalies of hydrothermal Fe–Mn oxides have been reported from settings such as MOR<sup>37,38</sup>, volcanic arc<sup>31,36</sup>, back arc<sup>8,39</sup>, and hot spot<sup>40</sup>. The absence of positive Eu anomalies in our samples (Fig. 3) suggests that fluid–rock interactions occurred at temperatures of  $<200$  °C<sup>34,35</sup>.

Because the Pb isotopic compositions of dredged Fe–Mn oxide samples differ from those of petit-spot lavas but are similar to those of presently forming hydrogenetic Fe–Mn crusts, the Pb in

our samples is inferred to be obtained from seawater. In MOR settings, rocks are strongly altered by high-temperature hydrothermal fluids such that the Pb isotopic compositions of their hydrothermal Fe–Mn oxides lie between those of MOR basalts (MORBs) and seawater (hydrogenetic Fe–Mn crusts)<sup>41</sup>. The Pb isotopic compositions of Fe–Mn oxides from low-temperature hydrothermal fields approximate those of seawater<sup>42,43</sup>. The seawater-like Pb isotopic compositions of our samples indicate that the hydrothermal alteration of petit-spot lava does not

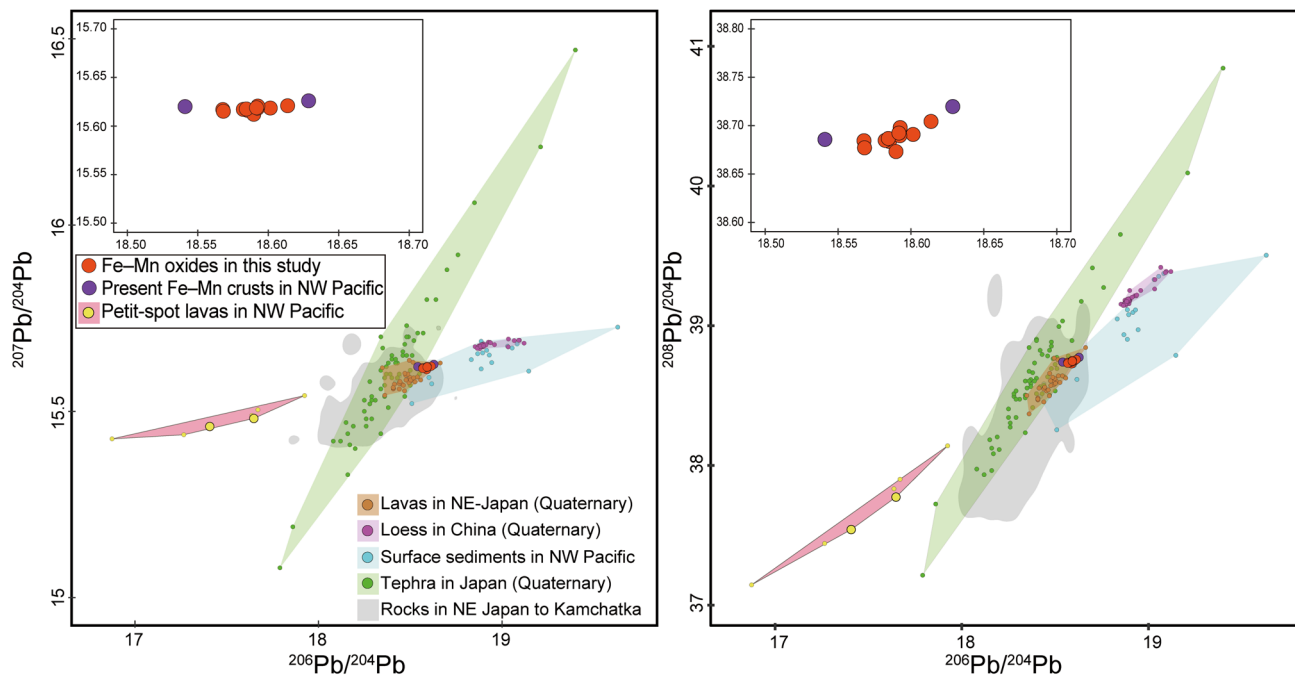


**Fig. 4 Pb isotopic compositions of Fe–Mn oxides.** Data for the Fe–Mn oxide samples (red dots), petit-spot lava samples (large yellow dots), and presently forming hydrogenetic Fe–Mn crusts (purple dots) around the study area. Data for petit-spot lavas in the NW Pacific Ocean<sup>70</sup> (small yellow dots), Quaternary tephra in Japan<sup>71</sup> (green dots), Quaternary lavas in NE Japan<sup>72</sup> (brown dots), Quaternary loess in China<sup>73,74</sup> (magenta dots), surface sediments in the NW Pacific Ocean<sup>73,75,76</sup> (cyan dots), and rocks from NE Japan to Kamchatka compiled in the GEOROC database (<http://georoc.mpch-mainz.gwdg.de/georoc/>) (gray field) are observed. The GEOROC data are shown as a probability density distribution (within 2σ) obtained from the kernel density estimation.

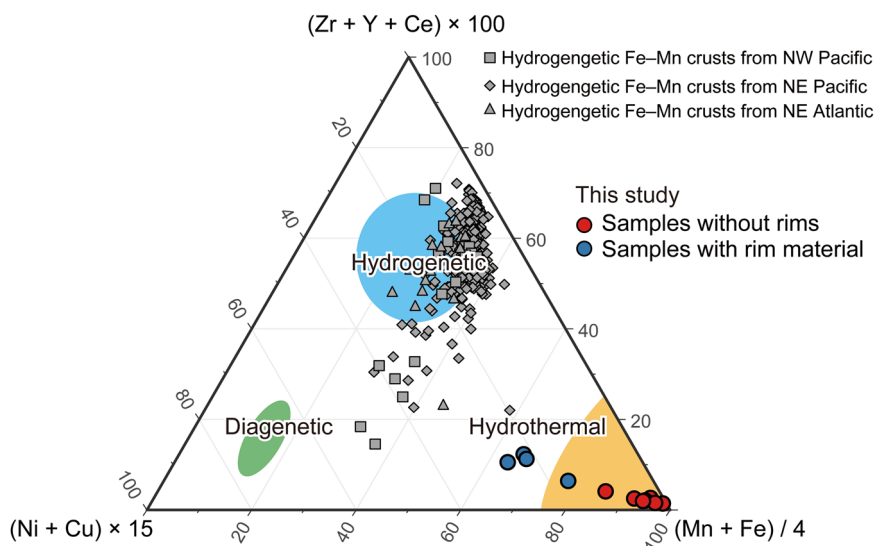


**Fig. 5 Ternary diagram to discriminate the origins of submarine Fe–Mn oxides.** The origins of submarine Fe–Mn oxides can be discriminated based on their chemical compositions<sup>24</sup>. Samples without rims (red dots) plot within the hydrothermal field origin (orange field)<sup>24</sup>, whereas samples containing rim material (blue dots) plot between the hydrothermal field and intermediate field of hydrogenetic (cyan area)<sup>24</sup> and diagenetic origins (green area)<sup>24</sup>. Gray squares, rhombuses, and triangles represent hydrogenetic Fe–Mn crusts collected from the NW Pacific Ocean<sup>17,25</sup>, NE Pacific Ocean<sup>26</sup>, and NE Atlantic Ocean<sup>27</sup>, respectively.

release Pb because fluid–rock interactions occur at low temperatures; alternatively, Pb might rapidly precipitate from hydrothermal fluids during upwelling.

The samples contain silicate debris cemented by Fe–Mn oxides but lava substrates are absent (Fig. 2), indicating that hydrothermal fluids diffused through and altered the seafloor sediments. This result supports a model involving low-

temperature hydrothermal activity on a sediment-covered seafloor<sup>8,31,36</sup>. To summarize, the mineralogy, chemical compositions, Pb isotope ratios, and textures of the samples can only be explained by low-temperature hydrothermal activity (probably at a petit-spot volcano) and suggest that the hydrothermal alteration of oceanic crust by petit-spot would be weaker than that by MOR, volcanic arc, back-arc, and hot spot.

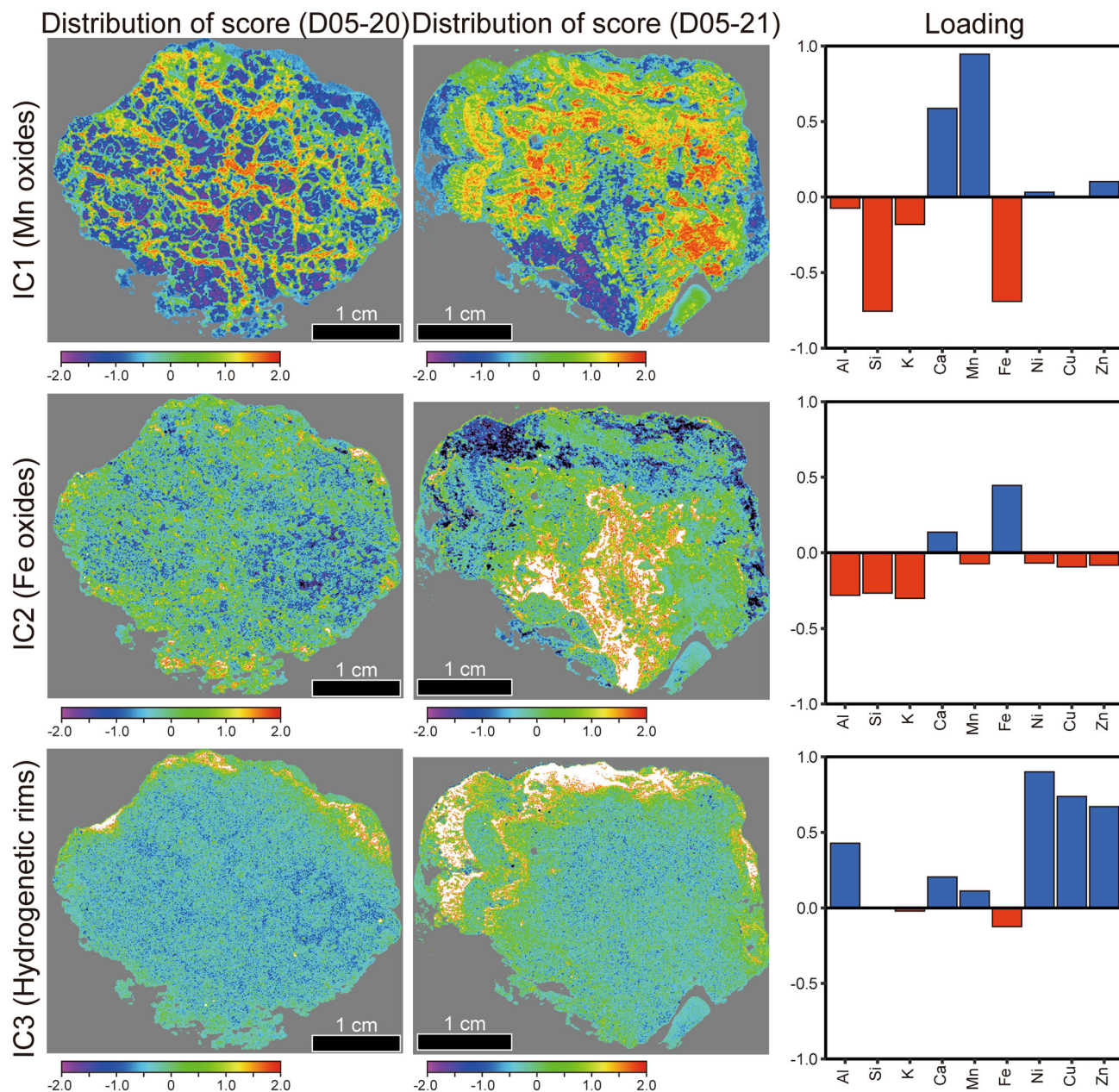


**Fig. 6 Scores and loadings of IC1, IC2, and IC3.** Scores and loadings show IC signal intensities in each pixel and the relative contributions of each element to the individual ICs, respectively. The gray areas in the distribution images of IC scores were trimmed prior to performing ICA (“Methods” for details). The white areas in the distribution images indicate regions in which the score exceeded 2.0.

**Formation process of hydrothermal Fe–Mn oxides.** We performed ICA using elemental mapping data (Al, Si, K, Ca, Mn, Fe, Ni, Cu, and Zn intensities are shown in Fig. 2 and Supplementary Fig. 3) obtained from micro-XRF to establish the hydrothermal Fe–Mn oxide formation process as well as the evolution of hydrothermal activity based on sample texture and geochemistry. ICA is a statistical method that estimates the original signals from observed multivariate data comprising statistically independent non-Gaussian source signals<sup>44</sup>. When applied to geochemical data, ICA can extract signatures of source materials or physico-chemical processes controlling the chemical compositions of samples as independent components (ICs)<sup>45,46</sup>.

Six ICs were extracted from elemental mapping data using ICA, the results of which can be presented as IC scores and IC loadings<sup>46</sup> (Fig. 6, Supplementary Fig. 4, and Supplementary Table 3)<sup>47</sup>. The value of each score represents the signal intensity

of an IC in each pixel of the elemental map. The IC loading shows the relative contribution of each element to the individual ICs<sup>46</sup> (“Methods” for details). The ICs are geochemically interpreted based on their score distributions and loading patterns. The caveat is that, although the extracted ICs are named as IC1–IC6, they cannot be ranked by their contributions to the data structure (i.e., by their proportional contribution to sample variance) because they are mutually independent; as such, their relative importance cannot be measured<sup>44,45</sup>. Therefore, the ordering determined is nominal and cannot be interpreted as a ranking or list of respective importance. The geochemical significance of each extracted IC is then described as follows.

IC1 is characterized by the positive loadings of Mn and Ca and the negative loadings of Fe and Si (Fig. 6). Because todorokite contains Ca as an interlayer cation<sup>28</sup>, the Mn oxides on the positive side of IC1 are associated with the hydrothermal activity,

whereas the negative side of IC1 reflects Si–Fe-rich materials. The Si–Fe rich material, recognized as the dark green or gray–brown portions of Fig. 2, is possibly silicate debris affected by low-temperature (<150 °C) hydrothermal alteration, which yields gray–green or dusky red clay and Fe oxyhydroxides<sup>48</sup>. Thus, IC1 extracts the compositional variation between the Si–Fe rich material and Mn oxides, both of which are produced by hydrothermal activity.

IC2 shows a distinct positive loading of Fe (Fig. 6), denoting Fe oxides decoupled from the negative side of IC1. The XRD analysis of the bulk sample powder showed no specific Fe minerals, indicating that the intense Fe signal arises from amorphous Fe (oxyhydr)oxides, which are plausibly of hydrothermal origin. The opposite signs of Fe and Si loadings in IC2 show that IC2 extracts Fe associated with hydrothermal processes that do not involve Si. Assuming this inference, the elemental maps of Fe and Si demonstrate different spatial distributions in the central and bottom left regions of D05-21 (Fig. 2), indicating that only a portion of Fe is closely associated with Si.

Note that IC3 is characterized by the positive loadings of Ni, Cu, and Zn, i.e., elements enriched in hydrogenetic Fe–Mn crusts, with high scores on the sample rims (Fig. 6). The columnar structure of the rim (Fig. 2) is recognized in hydrogenetic Fe–Mn crusts. The mineralogy and chemistry of powdered samples, including the rim material, demonstrates its hydrogenetic origin. As such, IC3 shows a hydrogenetic component that accumulates metals from ambient seawater. Metal accumulation in hydrogenetic components is a longer-term process than the growth of Fe–Mn oxides of hydrothermal origin.

Unlike IC1–IC3, IC4–IC6 do not appear to be linked to the Fe–Mn oxides. IC4, characterized by positive loadings of Si, Al, and Ca (Supplementary Fig. 4), possibly reflects aluminosilicate debris, such as clay and plagioclase, which were detected by XRD analysis. IC5 scores are extremely high (~10) for K-rich particles (possibly phillipsite) in D05-21 (Supplementary Fig. 3) and show an exclusively positive loading of K (Supplementary Fig. 4), reflecting variations in the K contents of the samples. This is attributed to compositional variations in the original detrital materials or elemental migration during hydrothermal alteration. IC6 loadings indicate that the intensities of all elements decrease with an increase in IC6 score. Moreover, the distribution of IC6 scores closely traces the surface ruggedness of these sectioned samples (Supplementary Fig. 4). Therefore, IC6 is considered to reflect the analytical error associated with X-ray focusing and shows that the influence of analytical error is separate from that of other ICs.

Based on the three key ICs described above (i.e., IC1–IC3), the processes of formation of the studied Fe–Mn oxides can be constrained. Differences (decoupling) in the spatial distributions of IC1 and IC2 scores (Fig. 6) indicate that Mn oxides and Fe oxides were formed by different processes. Because IC3 shows hydrogenetic rims, the upper side of the samples showing high IC3 scores in Fig. 6 were possibly exposed to seawater. In general, the formation of Fe–Mn oxides associated with low-temperature hydrothermal fluid diffusing through sediments has been proposed as follows<sup>8,31,36</sup>. First, when hydrothermal fluid ascending through the sediment column reaches the seafloor, Fe–Mn oxides are precipitated at the sediment–seawater interface where they cement the sediments. This Fe–Mn oxide layer becomes a cap that limits the exit of the subsequent upwelling fluid such that Fe–Mn oxides then grow downward in the sediment. Because of the abovementioned process, the area of highly positive IC2 scores underlying positive IC1 scores in sample D05-21 (Fig. 6) show that Fe oxides (IC2) precipitated when the upwelling hydrothermal fluids were obstructed by a capping layer of Mn oxides (IC1). The intrusion of an ascending

hydrothermal fluid in an Mn-oxide capping layer, followed by Fe oxide precipitation, has been reported in other hydrothermal fields<sup>8</sup>. The reticular distribution of Mn oxides (positive IC1 scores) in turn in sample D05-20 suggests that silicate debris was cemented by Mn oxides obtained from hydrothermal fluids that infiltrated these sediments. The absence of Fe oxides with highly positive IC2 scores in sample D05-20 may be attributed to limited sampling (only the cap layer was sampled), as is suggested by the appearance of a slightly positive IC2 at the very bottom of the sample.

To estimate the duration of hydrothermal activity, we calculated the growth rate of samples without their hydrogenetic rims. The growth rates of Fe–Mn oxides can be calculated from their chemical compositions using two methods, one based on Co<sup>49</sup> and another based on Ce<sup>50</sup>. We selected the Ce-chronology (“Methods” for details) because of gross disagreements between Co-chronology and U–Th dating that have previously been recognized in low-temperature hydrothermal Fe–Mn oxides<sup>36</sup>. The estimated growth rates (0.36–1.73 mm/kyr) and durations (19.0–76.3 kyr) in our petit-spot samples (Supplementary Table 1) were of the same order of magnitude as those of low-temperature hydrothermal Fe–Mn oxides in the Izu-Ogasawara Arc, previously estimated from U–Th dating<sup>36</sup>.

In summary, the hydrothermal activity forming the samples likely occurred via the following process (Fig. 7). Heat source magma (probably petit-spot magma) yielded low-temperature hydrothermal fluid by fluid–rock interactions at temperatures of <200 °C. The hydrothermal fluid ascended via the sediment column and precipitated Mn oxides at the sediment–seawater interface. Fe oxides were precipitated below the capping layer of Mn oxides. The hydrothermal fluid caused the alteration and cementation of silicate debris to Fe–Mn oxides. The duration of this hydrothermal process was 19.0–76.3 kyr. After this period of hydrothermal activity, a hydrogenetic rim formed on the side of the rock exposed to seawater.

**Implications for elemental fluxes in the ocean.** Because petit-spot volcanism in this study shares multiple geological features with previously studied examples<sup>9,10,14</sup>, we infer that hydrothermal activity should be a common phenomenon at petit-spot volcanoes. Because our samples formed on the sediment-covered seafloor, hydrothermal activity may have occurred at the foot of volcanoes rather than at their peaks, which are covered with volcanic rocks<sup>9,51</sup>. When evaluating the input of elements to the ocean from the petit-spot hydrothermal activity, we must estimate the water volume flux. Herein, we adopted a geophysical method previously used for estimating heat and water volume fluxes from MORs<sup>3,52</sup> (“Methods” for details). Based on the potential temperature of the asthenospheric source mantle (1300 °C), the temperature of petit-spot magmas was assumed to be 1220 °C<sup>11,52</sup>. Using seismic<sup>51</sup> and age<sup>9</sup> data from petit-spot volcanoes, the volume flux of petit-spot magma in the surveyed area (Fig. 1) was estimated to be  $5.0 \times 10^{-5}$  km<sup>3</sup>/yr. Assuming that all heat from this magma produced hydrothermal fluids with temperatures of 5–50 °C, the heat flux of the hydrothermal systems related to petit spots in the surveyed area would be  $7.0\text{--}7.2 \times 10^6$  W. The water volume flux was estimated to be  $1.1\text{--}19 \times 10^9$  kg/yr, similar to that of the Rainbow hydrothermal field on the Mid-Atlantic Ridge, although the corresponding heat flux was two orders of magnitude smaller<sup>53</sup>. Assuming that petit-spot volcanoes are as common near all trenches (~40,000 km)<sup>54</sup> similar to those in the study area, we estimated the global heat and water volume fluxes from petit-spot hydrothermal systems to be  $1.8 \times 10^9$  W and  $2.9\text{--}48 \times 10^{11}$  kg/yr, respectively, ~0.1% and several percent of those along the global MOR axis, respectively (Supplementary Table 4).

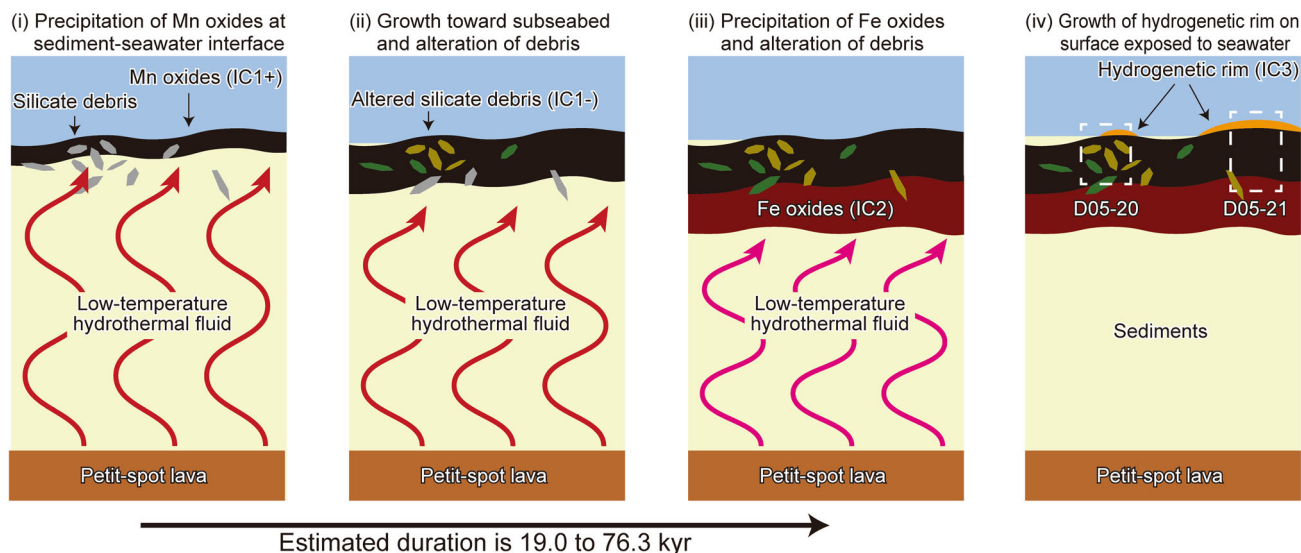


**Fig. 7 Schematic of hydrothermal activity inferred from this study.** (i) A low-temperature hydrothermal fluid is produced by fluid-rock interactions at temperatures of  $<200\text{ }^{\circ}\text{C}$  via the heat transfer, probably from petit-spot lava. Hydrothermal fluids diffuse through sediments and precipitate Mn oxides (IC1 positive) at the sediment-seawater interface. (ii) Downward growth of Mn oxides impedes the escape of ascending hydrothermal fluids. (iii) Fe oxides are precipitated beneath the Mn oxide cap layer. During the hydrothermally active period (19.0–76.3 kyr), silicate debris is altered by the hydrothermal fluid. (iv) A hydrogenetic rim (IC3) grows at the surface exposed to seawater. The absence of a highly positive IC2 score in sample D05-20 can be explained by partial (insufficient) sampling (*cf.* the white dashed boxes around samples D05-20 and D05-21).

This estimated water volume flux suggests that petit-spot hydrothermal systems exert a nonnegligible influence on the material input to the ocean. The magnitude of this influence depends on the chemistry of the hydrothermal fluid, which can be confirmed from the tectonic setting and chemical composition of the associated magma. Our samples indicate that hydrothermal fluids associated with petit-spot lava diffused via the seafloor sediment. Hydrothermal fluids traversing through sediments tend to be up to two orders of magnitude more enriched in  $\text{CH}_4$  and  $\text{NH}_3$  than those emanating from sediment-free crusts<sup>5</sup>. The concentrations of organic matter (from which the  $\text{CH}_4$  originates) in deep-sea sediments near trenches<sup>55</sup> are same order to those in the Okinawa Trough<sup>56</sup> of which host  $\text{CH}_4$ -rich hydrothermal fluids. Moreover, the volatiles of magmatic origin are also an important factor controlling the chemical composition of hydrothermal fluids<sup>5</sup>. Petit-spot magmas are extremely volatile-rich, with pre-degassing  $\text{CO}_2$  contents of 5–10 wt%<sup>12</sup> (10–100 times that of typical MORBs<sup>57</sup>). Therefore, hydrothermal fluids from petit-spot volcanoes may be rich in  $\text{CH}_4$ ,  $\text{NH}_3$ , and  $\text{CO}_2$ , indicating that petit-spot hydrothermal systems emit hydrothermal fluids containing certainly Fe and Mn and possibly  $\text{CH}_4$  and  $\text{NH}_3$ , thus providing potentially habitable zones for chemosynthetic bacteria. Moreover, owing to the  $\text{CO}_2$ -rich hydrothermal fluid and high water pressure at such depths, active hydrothermal vents may be accompanied by pools of liquid  $\text{CO}_2$  and  $\text{CO}_2$  hydrates as observed in the Okinawa Trough<sup>58</sup>, which are habitable for specific microbial groups<sup>58</sup>. By assuming that the  $\text{CO}_2$  and  $\text{CH}_4$  contents in petit-spot hydrothermal fluids were enriched to levels ten times those of MOR hydrothermal fluids, we roughly estimated that global emissions from the petit-spot systems would be  $1.7\text{--}80 \times 10^{11}$  mol/yr of  $\text{CO}_2$  and  $0.7\text{--}48 \times 10^9$  mol/yr of  $\text{CH}_4$ . These values are over several tens of percent comparing to those from MOR axis regions<sup>3</sup>, suggesting that elemental fluxes from petit-spot hydrothermal activity may play an important role in global geochemical cycles, particularly that of carbon.

As proposed in this study, petit-spot hydrothermal activity has the potential to be habitable zones for chemosynthetic bacteria on

old and cold oceanic crust and should form the deepest example of a hydrothermal field known to date. Because presently active petit-spot hydrothermal fields have not been confirmed yet, in order to reveal the physical and chemical properties of hydrothermal fluids in petit-spot hydrothermal systems, it is necessary to discover an active petit-spot hydrothermal site for in situ observations or to replicate the hydrothermal fluids by hydrothermal experiments.

## Methods

**Bulk chemical and mineralogical analyses.** Eight dredge samples were powdered for bulk chemical and mineralogical analyses as follows. Three samples containing a rim of hydrogenetic Fe–Mn oxides (D05-13, D05-15, and D05-21) were cut into subsamples with and without the rim material (sample D05-19 contained rim material but was not divided). After polishing the cut sections and soaking them in ultrapure water for  $\sim 12$  h, they were rinsed at least twice with ultrapure water, air-dried, pulverized in an agate mortar, and dried at  $110\text{ }^{\circ}\text{C}$ . The bulk chemical compositions of samples were measured by XRF (Primus II, Rigaku, Tokyo, Japan) and inductively coupled plasma mass spectrometry (ICP–MS; iCAP-Q, Thermo Fisher Scientific, Bremen, Germany) at The University of Tokyo following the methods described by Kato et al.<sup>59</sup>. Powder XRD analysis was performed using an Ultima IV instrument (Rigaku, Tokyo, Japan) with  $\text{CuK}\alpha$  radiation (40 kV and 30 mA) at The University of Tokyo. The scan range was  $2\theta = 3^{\circ}\text{--}75^{\circ}$  at a scan rate of  $1^{\circ}\text{min}^{-1}$ . The peaks of vernadite and birnessite overlapped at 2.4 and 1.4 Å, respectively. The intensity ratios of two birnessite peaks ( $3.5\text{ Å}/7.2\text{ Å}$ ) were extremely similar (0.18–0.20) in all samples, but the intensity ratios of the 2.4 and 7.2 Å peaks were higher in the rimmed samples than in samples without rims (Supplementary Fig. 1), indicating that vernadite resides in the rims.

**Micro-XRF analysis.** Elemental imaging of Al, Ca, Cu, Fe, K, Mg, Mn, Ni, Rb, S, Si, and Zn was performed on polished cross sections of samples D05-20 and D05-21 using micro-XRF (XGT7000V, Horiba, Kyoto, Japan) with energy-dispersive X-ray spectroscopy at Kyoto University. The analysis was repeated 15 times at a tube voltage of 50 kV, a tube current of 0.9 A, and an X-ray beam diameter of 100  $\mu\text{m}$ . Scanning was performed in  $\sim 75\text{ }\mu\text{m}$  intervals (pixel size) at a rate of 9 ms/pixel. The intensity was determined as the cumulative intensity of the 15 analyses (total analysis time = 135 ms/pixel).

**Pb isotopic composition analysis.** We analyzed the Pb isotopic compositions of hydrothermal Fe–Mn oxides, petit-spot lavas, and presently forming Fe–Mn crusts. The petit-spot lavas (D01-12 and D05-01) were obtained from the study area during cruise KS-18-9. The presently forming Fe–Mn crusts (D3-003T and D4-02T) were obtained from the surface layers ( $<5$  mm thick) of hydrogenetic Fe–Mn crusts



collected from the Joban Seamounts during cruise KH-92-3 and the Ojin Rise Seamounts east of Shatsky Rise during cruise KR14-07, respectively. Pb isotopic compositions were obtained using a multicollector ICP-MS (MC-ICP-MS; Neptune Plus, Thermo Fisher Scientific, Bremen, Germany) at Chiba Institute of Technology. Fe-Mn samples were leached in 6-N HCl at 80 °C for 15 min, which did not dissolve the silicate debris<sup>60</sup>. After separating undissolved materials from the solution by centrifugation (~1460 G for 5 min), the solubilized Pb was separated in an anion-exchange resin with Tl doping for mass-bias correction. The Pb separation and analytical procedure are described in Tanimizu and Ishikawa<sup>61</sup>. In repeated analyses of the isotopic standard NIST SRM981 Pb, the measurement reproducibility ( $2\sigma$ ) was  $^{206}\text{Pb}/^{204}\text{Pb} = 16.9315 \pm 0.0006$ ,  $^{207}\text{Pb}/^{204}\text{Pb} = 15.4849 \pm 0.0009$ , and  $^{208}\text{Pb}/^{204}\text{Pb} = 36.6768 \pm 0.0019$  ( $n = 3$ ). The total procedural blank of Pb yielded a negligibly small value (13.4 pg). Pb recovery yield in Fe-Mn oxides exceeded 90%.

**ICA.** The theoretical background, numerical methods, and geochemical applications of ICA are detailed elsewhere<sup>44–46</sup>. We first trimmed the elemental mapping data (Supplementary Data 1–2) to omit data from outside the sample surface. This trimming was based on the intensities of the major elements (K < 5 counts, Al < 5 counts, Si < 20 counts, Mn < 50 counts, and Fe < 50 counts). The omitted data are shown as gray areas in Fig. 6 and Supplementary Fig. 4. Because ICA presupposes non-Gaussian distributions of the original signals, we verified the data structure. The histograms of elemental intensities were multimodal, concave, or long-tailed, reflecting inherent non-Gaussian data distributions (Supplementary Fig. 5). This result justifies the application of ICA to our data.

ICA was implemented using the “fastICA” function in the “fastICA” package developed for ICA in R. In the numerical process, the observed ICA data  $\mathbf{X}$  are expressed as a matrix of  $n \times m$ , in which the rows and columns correspond to the data points (i.e., pixels) and observed variables (counts of each element), respectively, as follows:

$$\mathbf{X} = \mathbf{S}\mathbf{A}, \quad (1)$$

where  $\mathbf{S}$  is an independent source of an  $n \times r$  matrix (whose columns are ICs), and  $\mathbf{A}$  is an  $r \times m$  mixing matrix. The  $\mathbf{S}$  matrix estimated by ICA is the IC signal intensities in each observed pixel (defined as the score), and  $\mathbf{A}$  is the relative contributions of each element to the individual ICs (defined as the loading<sup>46</sup>).  $r$  is the number of ICs to be extracted, which can be selected as an integer between 1 and  $m$  inclusive. In this study,  $r$  was set to six, denoting that 90.7% of the total data variance could be collectively explained by the six ICs. After centering  $\mathbf{X}$  as per the mean of each variable, the unknown  $\mathbf{S}$  was obtained as follows:

$$\mathbf{S} = \mathbf{X}\mathbf{K}\mathbf{W}, \quad (2)$$

where  $\mathbf{K}$  is a whitening matrix and  $\mathbf{W}$  is an orthogonal matrix for rotating the whitened data. The columns of whitened  $\mathbf{X}$  have zero mean and unit variance and are uncorrelated.  $\mathbf{W}$  is numerically determined to maximize the non-Gaussianity of each whitened variable using an evaluation function approximating negentropy<sup>44</sup>. The histograms of extracted IC scores demonstrate strongly non-Gaussian distributions, thus confirming the mutual independence of the extracted components<sup>44,46</sup> (Supplementary Fig. 6 and Supplementary Data 3–4).

**Growth rate estimation.** The growth rates of submarine Fe-Mn oxides can be estimated from their Co<sup>49</sup> or Ce<sup>50</sup> components. Co-based chronology, which assumes a constant nondetrital Co flux to the seafloor, is extensively applied; however, in addition to the GEOTRACES program having demonstrated that nondetrital Co flux to the seafloor varies<sup>62</sup>, particularly near continental margins (where our study area is located); its results for low-temperature hydrothermal Fe-Mn oxides are inconsistent with those of U-Th dating (the discrepancy factor is ~100)<sup>36</sup>. Furthermore, Ce-based chronology estimates growth rates (GR in mm/Myr) from Ce enrichment in Fe-Mn oxides with respect to ambient seawater as follows:

$$\text{GR} = \frac{1.94 \times 10^4}{(C_{\text{EM}} - C_{\text{SW}} \times Pr_{\text{EM}}/Pr_{\text{SW}})^{1.43}}, \quad (3)$$

where  $C_{\text{EM}}$ ,  $Pr_{\text{EM}}$ ,  $C_{\text{SW}}$ , and  $Pr_{\text{SW}}$  are Ce and Pr contents ( $\mu\text{g/g}$ ) of Fe-Mn oxides and ambient seawater, respectively<sup>50</sup>. Therefore, we employed the Ce-based chronology with respect to the measured REY composition of the ambient seawater<sup>63</sup>.

**Estimation of heat and water volume fluxes.** The heat and water volume fluxes from the petit-spot hydrothermal system were estimated using geophysical methods<sup>3,52</sup>. Based on its P-wave velocity, the oceanic crust is conventionally divided into three layers: layer 1 (sediment), layer 2 (pillow lavas and dolerite sheet dikes), and layer 3 (gabbroic lower crust)<sup>64</sup>. After deriving the conical volume in layer 1 and columnar volume in layer 2 from seismic data<sup>51</sup>, the magma volume of a single petit-spot volcano above layer 3 (shallower than 2.5 km below the seafloor<sup>65</sup>) was calculated as  $3.3 \text{ km}^3$  (Supplementary Fig. 7). The magma volume flux ( $F_V$ ) of petit-spot volcanism in the surveyed area was  $5.0 \times 10^{-5} \text{ km}^3/\text{yr}$ . The estimation formula was as follows:

$$F_V = V \times N/A, \quad (4)$$

where  $V$  is the magma volume of a single volcano,  $N$  is the number of volcanoes in

the surveyed area<sup>14</sup>, and  $A$  is the oldest age of the petit-spot volcanoes<sup>9</sup> (Supplementary Table 4). Assuming that all heat in the petit-spot magma was consumed by hydrothermal fluid production ( $T_H = 5\text{--}50 \text{ }^\circ\text{C}$ ), the hydrothermal heat flux ( $F_H$ ) and water volume flux ( $F_W$ ) were  $7.0\text{--}7.2 \times 10^6 \text{ W}$  and  $1.1\text{--}19 \times 10^9 \text{ kg/yr}$ , respectively. The estimation formulas are as follows:

$$F_H = F_V \{ \rho c_m (T_m - T_H) + L \}, \quad (5)$$

$$F_W = F_H / \{ c_H (T_H - T_s) \}, \quad (6)$$

where  $\rho c_m$  is the volume-specific heat of magma ( $3.8 \times 10^6 \text{ J/m}^3/\text{K}$ )<sup>52</sup>,  $T_m$  is the intrusion temperature ( $1220 \text{ }^\circ\text{C}$ ),  $L$  is the latent heat per volume of magma ( $10,280 \text{ J/m}^3$ )<sup>52</sup>,  $c_H$  is the specific heat of the hydrothermal fluid ( $4 \text{ J/g/K}$ )<sup>66</sup>, and  $T_s$  is seawater temperature ( $2 \text{ }^\circ\text{C}$ ). Because the potential temperature of the asthenosphere under petit-spot volcanoes is  $\sim 1300 \text{ }^\circ\text{C}$ <sup>11</sup>, the intrusion temperature of the petit-spot magma was set to the temperature of dolerite dikes in MOR<sup>52</sup>. The global magma volume flux of petit-spot volcanism can be estimated from the percentage of the area near the trench represented by the surveyed area (Fig. 1), the length of the surveyed area along the trench<sup>12</sup>, and the total length of all trenches<sup>54</sup> (Supplementary Table 4) if the occurrence frequency of petit-spot volcanism in the study area is representative of other trenches. This calculation yields a global heat flux of  $1.8 \times 10^9 \text{ W}$  and a global water volume flux of  $2.9\text{--}48 \times 10^{11} \text{ kg/yr}$ .

## Data availability

The authors declare that the data supporting the findings of this study are available in the Figshare database under Digital Object Identifier. <https://doi.org/10.6084/m9.figshare.22559677.v1> (elemental mapping data: Fig. 2 and Supplementary Figs. 3 and 5) <https://doi.org/10.6084/m9.figshare.22559803.v1> (chemical, mineral, and Pb isotopic compositions: Figs. 3–5, Supplementary Tables 1–2 and Supplementary Fig. 2) <https://doi.org/10.6084/m9.figshare.22559590.v1> (results of ICA: Fig. 6, Supplementary Fig. 4 and Supplementary Table 3) <https://doi.org/10.6084/m9.figshare.22559851.v1> (XRD intensity: Supplementary Fig. 1)

## Code availability

We have provided a full code available in the paper.

Received: 29 July 2022; Accepted: 28 April 2023;

Published online: 01 June 2023

## References

- Beaulieu, S. E., Baker, E. T., German, C. R. & Maffei, A. An authoritative global database for active submarine hydrothermal vent fields. *Geochem. Geophys. Geosyst.* **14**, 4892–4905 (2013).
- Rona, P. A. Hydrothermal mineralization at seafloor spreading centers. *Earth Sci. Rev.* **20**, 1–104 (1984).
- Elderfield, H. & Schultz, A. Mid-ocean ridge hydrothermal fluxes and the chemical composition of the ocean. *Annu. Rev. Earth Planet. Sci.* **24**, 191–224 (1996).
- Hannington, M. D. The role of black smokers in the Cu mass balance of the oceanic crust. *Earth Planet. Sci. Lett.* **374**, 215–226 (2013).
- Nakamura, K. & Takai, K. Theoretical constraints of physical and chemical properties of hydrothermal fluids on variations in chemolithotrophic microbial communities in seafloor hydrothermal systems. *Prog. Earth Planet. Sci.* **1**, 5 (2014).
- Bruland, K. W., Middag, R. & Lohan, M. C. Controls of Trace Metals in Seawater. In *Treatise on Geochemistry* (eds. Holland, H. D. & Turekian, K. K. B. T.-T. on G. (Second E.) 19–51 (Elsevier, 2014). <https://doi.org/10.1016/B978-0-08-095975-7.00602-1>.
- Sander, S. G. & Koschinsky, A. The export of iron and other trace metals from hydrothermal vents and the impact on their marine biogeochemical cycle. In *Trace Metal Biogeochemistry and Ecology of Deep-Sea Hydrothermal Vent Systems* (eds. Demina, L.L. & Galkin, S.V.) 9–24 (Springer International Publishing, 2016). [https://doi.org/10.1007/698\\_2016\\_4](https://doi.org/10.1007/698_2016_4).
- Pelleter, E. et al. Ni-Cu-Co-rich hydrothermal manganese mineralization in the Wallis and Futuna back-arc environment (SW Pacific). *Ore Geol. Rev.* **87**, 126–146 (2017).
- Hirano, N. et al. Volcanism in response to plate flexure. *Science*. **313**, 1426–1428 (2006).
- Hirano, N. & Machida, S. The mantle structure below petit-spot volcanoes. *Commun. Earth Environ.* **3**, 110 (2022).
- Machida, S., Kogiso, T. & Hirano, N. Petit-spot as definitive evidence for partial melting in the asthenosphere caused by  $\text{CO}_2$ . *Nat. Commun.* **8**, 14302 (2017).

12. Okumura, S. & Hirano, N. Carbon dioxide emission to Earth's surface by deep-sea volcanism. *Geology* **41**, 1167–1170 (2013).
13. Fujie, G. et al. Spatial variations of incoming sediments at the northeastern Japan arc and their implications for megathrust earthquakes. *Geology* **48**, 614–619 (2020).
14. Hirano, N., Koppers, A. A. P., Takahashi, A., Fujiwara, T. & Nakanishi, M. Seamounts, knolls and petit-spot monogenic volcanoes on the subducting Pacific Plate. *Basin Res.* **20**, 543–553 (2008).
15. Sedwick, P. N., McMurtry, G. M. & Macdougall, J. D. Chemistry of hydrothermal solutions from Pele's Vents, Loihi Seamount, Hawaii. *Geochim. Cosmochim. Acta* **56**, 3643–3667 (1992).
16. Akizawa, N. et al. A direct evidence for disturbance of whole sediment layer in the subducting Pacific plate by petit-spot magma–water/sediment interaction. *Mar. Geol.* **444**, 106712 (2022).
17. Azami, K., Hirano, N., Machida, S., Yasukawa, K. & Kato, Y. Rare earth elements and yttrium (REY) variability with water depth in hydrogenetic ferromanganese crusts. *Chem. Geol.* **493**, 224–233 (2018).
18. Nakanishi, M., Tamaki, K. & Kobayashi, K. Mesozoic magnetic anomaly lineations and seafloor spreading history of the northwestern Pacific. *J. Geophys. Res. Solid Earth* **94**, 15437–15462 (1989).
19. Grambow, B., Jercinovic, M. J., Ewing, R. C. & Byers, C. D. Weathered basalt glass: a natural analogue for the effects of REACTION progress on nuclear waste glass alteration. *MRS Proc.* **50**, 263 (1985).
20. Azami, K. et al. Elemental mapping data of the hydrothermal ferromanganese oxides obtained from a petit-spot volcano. *figshare* (2023) <https://doi.org/10.6084/m9.figshare.22559677.v1>.
21. Azami, K. et al. Chemical, mineral and Pb isotopic compositions of the hydrothermal ferromanganese oxides obtained from a petit-spot volcano and related materials. *figshare* (2023) <https://doi.org/10.6084/m9.figshare.22559803.v1>.
22. Taylor, S. R. & McLennan, S. M. *The continental crust: its composition and evolution*. (Blackwell Scientific Pub., 1985).
23. Azami, K. et al. X-ray diffraction intensities of the hydrothermal ferromanganese oxides obtained from a petit-spot volcano. *figshare* (2023) <https://doi.org/10.6084/m9.figshare.22559851.v1>.
24. Josso, P. et al. A new discrimination scheme for oceanic ferromanganese deposits using high field strength and rare earth elements. *Ore Geol. Rev.* **87**, 3–15 (2017).
25. Hein, J. R., Conrad, T. A., Frank, M., Christl, M. & Sager, W. W. Copper-nickel-rich, amalgamated ferromanganese crust-nodule deposits from Shatsky Rise, NW Pacific. *Geochem. Geophys. Geosyst.* **13**, Q10022 (2012).
26. Conrad, T., Hein, J. R., Paytan, A. & Clague, D. A. Formation of Fe–Mn crusts within a continental margin environment. *Ore Geol. Rev.* **87**, 25–40 (2017).
27. Koschinsky, A., Halbach, P., Hein, J. R. & Mangini, A. Ferromanganese crusts as indicators for paleoceanographic events in the NE Atlantic. *Geol. Rundschau* **85**, 567–576 (1996).
28. Usui, A., Mellin, T. A., Nohara, M. & Yuasa, M. Structural stability of marine 10 Å manganates from the Ogasawara (Bonin) Arc: Implication for low-temperature hydrothermal activity. *Mar. Geol.* **86**, 41–56 (1989).
29. Azami, K. et al. <sup>87</sup>Sr/<sup>86</sup>Sr isotopic ratio of ferromanganese crusts as a record of detrital influx to the Western North Pacific Ocean. *Minerals* **12**, 943 (2022).
30. Treffy, J. H. et al. Trace metals in hydrothermal solutions from Cleft segment on the southern Juan de Fuca Ridge. *J. Geophys. Res. Solid Earth* **99**, 4925–4935 (1994).
31. Hein, J. R., Schulz, M. S., Dunham, R. E., Stern, R. J. & Bloomer, S. H. Diffuse flow hydrothermal manganese mineralization along the active Mariana and southern Izu–Bonin arc system, western Pacific. *J. Geophys. Res. Solid Earth* **113**, B08S14 (2008).
32. Rogers, T. D. S., Hodkinson, R. A. & Cronan, D. S. Hydrothermal manganese deposits from the Tonga–Kermadec Ridge and Lau Basin region, Southwest Pacific. *Mar. Georesources Geotechnol.* **19**, 245–268 (2001).
33. Scholten, J. C. et al. Hydrothermal iron and manganese crusts from the pitcairn hotspot region. *Ocean. Hotspots* 375–405 (2004) [https://doi.org/10.1007/978-3-642-18782-7\\_13](https://doi.org/10.1007/978-3-642-18782-7_13).
34. Bau, M. Rare-earth element mobility during hydrothermal and metamorphic fluid rock interaction and the significance of the oxidation-state of europium. *Chem. Geol.* **93**, 219–230 (1991).
35. Bau, M. et al. Discriminating between different genetic types of marine ferromanganese crusts and nodules based on rare earth elements and yttrium. *Chem. Geol.* **381**, 1–9 (2014).
36. Yamaoka, K., Ma, L., Hishikawa, K. & Usui, A. Geochemistry and U-series dating of Holocene and fossil marine hydrothermal manganese deposits from the Izu–Ogasawara arc. *Ore Geol. Rev.* **87**, 114–125 (2017).
37. Dias, Á. S. C. M. A. & Barriga, F. J. A. S. Mineralogical and geochemical hydrothermal evidences on sediments from the serpentinite-hosted Saldanha hydrothermal field. *Miner. Depos. Meet. Glob. Chall.* 603–606 (2005) [https://doi.org/10.1007/3-540-27946-6\\_154](https://doi.org/10.1007/3-540-27946-6_154).
38. German, C. R. et al. Geochemistry of a hydrothermal sediment core from the OBS vent-field, 21 degrees N east pacific rise hydrothermal systems, alteration and ore deposition. *Chem. Geol.* **155**, 65–75 (1999).
39. Zeng, Z. et al. Formation of Fe–Si–Mn oxyhydroxides at the PACMANUS hydrothermal field, Eastern Manus Basin: mineralogical and geochemical evidence. *J. Asian Earth Sci.* **60**, 130–146 (2012).
40. Rouxel, O., Toner, B., Germain, Y. & Glazer, B. Geochemical and iron isotopic insights into hydrothermal iron oxyhydroxide deposit formation at Loihi Seamount. *Geochim. Cosmochim. Acta* **220**, 449–482 (2018).
41. van de Fliert, T. et al. Tracing the history of submarine hydrothermal inputs and the significance of hydrothermal hafnium for the seawater budget—a combined Pb–Hf–Nd isotope approach. *Earth Planet. Sci. Lett.* **222**, 259–273 (2004).
42. Godfrey, L. V. et al. The Hf isotopic composition of ferromanganese nodules and crusts and hydrothermal manganese deposits: Implications for seawater Hf. *Earth Planet. Sci. Lett.* **151**, 91–105 (1997).
43. Rehkämper, M. et al. Thallium isotope variations in seawater and hydrogenetic, diagenetic, and hydrothermal ferromanganese deposits. *Earth Planet. Sci. Lett.* **197**, 65–81 (2002).
44. Hyvärinen, A. & Oja, E. Independent component analysis: algorithms and applications. *Neural Netw.* **13**, 411–430 (2000).
45. Iwamori, H. & Albarède, F. Decoupled isotopic record of ridge and subduction zone processes in oceanic basalts by independent component analysis. *Geochem. Geophys. Geosyst.* **9**, Q04033 (2008).
46. Yasukawa, K., Nakamura, K., Fujinaga, K., Iwamori, H. & Kato, Y. Tracking the spatiotemporal variations of statistically independent components involving enrichment of rare-earth elements in deep-sea sediments. *Sci. Rep.* **6**, 29603 (2016).
47. Azami, K. et al. Results of independent component analysis for the elemental mapping data of the hydrothermal ferromanganese oxides obtained from a petit-spot volcano. *figshare* (2023) <https://doi.org/10.6084/m9.figshare.22559590.v1>.
48. Talbi, E. H. & Honnorez, J. Low-temperature alteration of mesozoic oceanic crust, Ocean Drilling Program Leg 185. *Geochem. Geophys. Geosyst.* **4**, 8906 (2003).
49. Manheim, F. T. & Lane-Bostwick, C. M. Cobalt in ferromanganese crusts as a monitor of hydrothermal discharge on the Pacific sea floor. *Nature* **335**, 59–62 (1988).
50. Kuhn, T., Bau, M., Blum, N. & Halbach, P. Origin of negative Ce anomalies in mixed hydrothermal–hydrogenetic Fe–Mn crusts from the Central Indian Ridge. *Earth Planet. Sci. Lett.* **163**, 207–220 (1998).
51. Fujiwara, T., Hirano, N., Abe, N. & Takizawa, K. Subsurface structure of the 'petit-spot' volcanoes on the northwestern Pacific Plate. *Geophys. Res. Lett.* **34**, 3–7 (2007).
52. Sleep, N. H. Hydrothermal circulation, anhydrite precipitation, and thermal structure at ridge axes. *J. Geophys. Res.* **96**, 2375 (1991).
53. German, C. R. et al. Heat, volume and chemical fluxes from submarine venting: a synthesis of results from the Rainbow hydrothermal field, 36°N MAR. *Deep. Res. Part 1 Oceanogr. Res. Pap.* **57**, 518–527 (2010).
54. Reymer, A. & Schubert, G. Phanerozoic addition rates to the continental crust and crustal growth. *Tectonics* **3**, 63–77 (1984).
55. Raimbourg, H. et al. Organic matter cracking: a source of fluid overpressure in subducting sediments. *Tectonophysics* **721**, 254–274 (2017).
56. Chang, Y.-P. et al. Foraminiferal oxygen isotope stratigraphy and high-resolution organic carbon, carbonate records from the Okinawa Trough (IMAGES MD012404 and ODP Site 1202). *Terr. Atmos. Ocean. Sci.* **16**, 57–73 (2005).
57. Le Voyer, M. et al. Carbon fluxes and primary magma CO<sub>2</sub> contents along the global mid-ocean ridge system. *Geochem. Geophys. Geosyst.* **20**, 1387–1424 (2019).
58. Inagaki, F. et al. Microbial community in a sediment-hosted CO<sub>2</sub> lake of the southern Okinawa Trough hydrothermal system. *Proc. Natl. Acad. Sci.* **103**, 14164–14169 (2006).
59. Kato, Y., Fujinaga, K. & Suzuki, K. Major and trace element geochemistry and Os isotopic composition of metalliferous umbers from the Late Cretaceous Japanese accretionary complex. *Geochem. Geophys. Geosyst.* **6**, Q07004 (2005).
60. van de Fliert, T. et al. Lead isotopes in North Pacific deep water – implications for past changes in input sources and circulation patterns. *Earth Planet. Sci. Lett.* **209**, 149–164 (2003).
61. Tanimizu, M. & Ishikawa, T. Development of rapid and precise Pb isotope analytical techniques using MC-ICP-MS and new results for GSJ rock reference samples. *Geochem. J.* **40**, 121–133 (2006).
62. Schlitzer, R. et al. The GEOTRACES intermediate data product 2017. *Chem. Geol.* **493**, 210–223 (2018).
63. Zhang, J. *Geochemistry of Yttrium and Lanthanides in seawater*. (The University of Tokyo, 1995). <https://doi.org/10.11501/3127036>.
64. White, R. S., McKenzie, D. & O'Nions, R. K. Oceanic crustal thickness from seismic measurements and rare earth element inversions. *J. Geophys. Res.* **97**, 19683 (1992).

65. Kodaira, S. et al. Seismological evidence of mantle flow driving plate motions at a palaeo-spreading centre. *Nat. Geosci.* **7**, 371–375 (2014).
66. Bischoff, J. L. & Rosenbauer, R. J. An empirical equation of state for hydrothermal seawater (3.2 percent NaCl). *Am. J. Sci.* **285**, 725–763 (1985).
67. Amante, C. & Eakins, B. W. ETOPO1 1 arc-minute global relief model: procedures, data sources and analysis. *NOAA Tech. Memo. NESDIS NGDC-24* 19 (2009) <https://doi.org/10.7289/V5C8276M>.
68. Wessel, P., Smith, W. H. F., Scharroo, R., Luis, J. & Wobbe, F. Generic mapping tools: improved version released. *Eos (Washington, DC)* **94**, 409–410 (2013).
69. Anders, E. & Grevesse, N. Abundances of the elements: meteoritic and solar. *Geochim. Cosmochim. Acta* **53**, 197–214 (1989).
70. Machida, S., Hirano, N. & Kimura, J. I. Evidence for recycled plate material in Pacific upper mantle unrelated to plumes. *Geochim. Cosmochim. Acta* **73**, 3028–3037 (2009).
71. Kimura, J.-I., Nagahashi, Y., Satoguchi, Y. & Chang, Q. Origins of felsic magmas in Japanese subduction zone: geochemical characterizations of tephra from caldera-forming eruptions <5Ma. *Geochem. Geophys. Geosyst.* **16**, 2147–2174 (2015).
72. Kimura, J. I. & Yoshida, T. Contributions of slab fluid, mantle wedge and crust to the origin of quaternary lavas in the NE Japan arc. *J. Petrol.* **47**, 2185–2232 (2006).
73. Jones, C. E., Halliday, A. N., Rea, D. K. & Owen, R. M. Eolian inputs of lead to the North Pacific. *Geochim. Cosmochim. Acta* **64**, 1405–1416 (2000).
74. Sun, J. & Zhu, X. Temporal variations in Pb isotopes and trace element concentrations within Chinese eolian deposits during the past 8 Ma: Implications for provenance change. *Earth Planet. Sci. Lett.* **290**, 438–447 (2010).
75. Pettke, T., Halliday, A. N. & Rea, D. K. Cenozoic evolution of Asian climate and sources of Pacific seawater Pb and Nd derived from eolian dust of sediment core LL44-GPC3. *Paleoceanography* **17**, 3-1–3–13 (2002).
76. Hemming, S. R. Y. & McLennan, S. M. Pb isotope compositions of modern deep sea turbidites. *Earth Planet. Sci. Lett.* **184**, 489–503 (2001).

## Acknowledgements

We thank the crews and scientific party of R/V Shinsei-Marui for assistance in sample collection and description during the cruise KS-18-9. Technical staff and students at our laboratories at The University of Tokyo and the Ocean Resources Research Center for Next Generation at the Chiba Institute of Technology are acknowledged for their assistance in performing geochemical analyses. This study was supported by the Japan Society for the Promotion of Science KAKENHI grants 18J21266 (K.A.), 18H03733 (N.H.), 17K05715 (N.H.), and 20H05658 (Y.K.).

## Author contributions

N.H., S.M., and K.A. collected the samples and designed the research plan. K.A. and S.M. analyzed mineralogy and geochemistry under supervision by T.K., K.N., and Y.K. M.N. analyzed bathymetric and acoustic data. K.A. performed ICA under supervision by K.Y. K.A. wrote the manuscript with contributions by other authors.

## Competing interests

The authors declare no competing interests.

## Additional information

**Supplementary information** The online version contains supplementary material available at <https://doi.org/10.1038/s43247-023-00832-3>.

**Correspondence** and requests for materials should be addressed to Keishiro Azami or Naoto Hirano.

**Peer review information** *Communications Earth & Environment* thanks the anonymous reviewers for their contribution to the peer review of this work. Primary Handling Editors: Derya Güner and Joe Aslin. Peer reviewer reports are available.

**Reprints and permission information** is available at <http://www.nature.com/reprints>

**Publisher's note** Springer Nature remains neutral with regard to jurisdictional claims in published maps and institutional affiliations.



**Open Access** This article is licensed under a Creative Commons Attribution 4.0 International License, which permits use, sharing, adaptation, distribution and reproduction in any medium or format, as long as you give appropriate credit to the original author(s) and the source, provide a link to the Creative Commons license, and indicate if changes were made. The images or other third party material in this article are included in the article's Creative Commons license, unless indicated otherwise in a credit line to the material. If material is not included in the article's Creative Commons license and your intended use is not permitted by statutory regulation or exceeds the permitted use, you will need to obtain permission directly from the copyright holder. To view a copy of this license, visit <http://creativecommons.org/licenses/by/4.0/>.

© The Author(s) 2023